Synthesis and Characterization of Ligand-Linked Pt Nanoparticles: Tunable, Three-Dimensional, Porous Networks for Catalytic Hydrogen Sensing

Daniel Loof,[a] Oliver Thüringer,[a] Marco Schowalter,[b] Christoph Mahr,[b] Anmona Shabnam Pranti,[c] Walter Lang,[c] Andreas Rosenauer,[b] Volkmar Zielasek,*[a] Sebastian Kunz,[a, d] and Marcus Bäumer[a]

Porous networks of Pt nanoparticles interlinked by bifunctional organic ligands have shown high potential as catalysts in micromachined hydrogen gas sensors. By varying the ligand among p-phenylenediamine, benzidine, 4,4''-diamino-p-terphenyl, 1,5-diaminonaphthalene, and trans-1,4-diaminocyclohexane, new variants of such networks were synthesized. Inter-particle distances within the networks, determined via transmission electron microscopy tomography, varied from 0.8 to 1.4 nm in accordance with the nominal length of the respective ligand. While stable structures with intact and coordinatively bonded diamines were formed with all ligands, aromatic diamines showed superior thermal stability. The networks exhibited mesoporous structures depending on ligand and synthesis strategy and performed well as catalysts in hydrogen gas microsensors. They demonstrate the possibility of deliberately tuning micro- and mesoporosity and thereby transport properties and steric demands by choice of the right ligand also for other applications in heterogeneous catalysis.

1. Introduction

Safe handling of hydrogen is of relevance for a multitude of industrial processes and technological applications. Being used as a reactant in large-scale production of ammonia, petrochemicals, and methanol or in Fischer Tropsch synthesis,[1–3] hydrogen gas is of increasing importance as a sustainable energy carrier in its own right, e.g., for fuel cells or automotive applications because it can be produced cleanly and easily by splitting abundant water via renewable energy sources such as wind or solar power. In fact, the 'National Hydrogen Strategy' of the Federal Government of Germany describes the scheduled transition of energy supply which relies on a large hydrogen infrastructure to be established in the future. Therefore, huge amounts of hydrogen may be present in our society as well as in the environment.[4]

Since hydrogen is a colorless and odorless gas with a wide flammable range of 4–75 vol.% in air and a low minimum ignition energy (0.017 mJ), transport, storage and use of hydrogen gas bear high risks. Any leakage may quickly lead to large volumes of explosive atmosphere due to fast diffusion of hydrogen in air (diffusion coefficient of 0.61 cm^2/s at ambient conditions).[1] Therefore, in any application or process in which hydrogen is present in larger scales, a fast and reliable detection of hydrogen is indispensable to quickly detect leaks in order to prevent accumulation. Consequently, quantification of hydrogen concentration in the range from the lower flammability limit (LFL) of 4% in air down to ppm levels is crucial for safety applications.[1]

Hydrogen gas sensing is furthermore interesting for medical applications. Since hydrogen is generated by intestinal bacteria at ppm levels, its concentration in human breath can reveal medically relevant information about the digestive system. Human breath may be a complex mixture of hydrogen and various other gases (e.g. H_2O, CH_4, CO, NH_4, CO_2, various volatile organic compounds (VOCs)).[5] Therefore, besides a fast response time and high sensitivity also high selectivity for hydrogen gas sensing is of high demand.

At present, three different types of hydrogen gas sensors are commercially available, namely palladium gate metal-oxide-silicon field-effect transistors (MOSFET), metal oxide semiconductor (MOS) sensors, and catalytic combustion devices.[3,5–8] A major disadvantage of MOS-based sensors and non-micro-

[a] D. Loof, O. Thüringer, Dr. V. Zielasek, Dr. S. Kunz, Prof. Dr. M. Bäumer
Institute of Applied and Physical Chemistry
University of Bremen
Leobener Str. 6
28359 Bremen (Germany)
E-mail: zielasek@uni-bremen.de
[b] Dr. M. Schowalter, Dr. C. Mahr, Prof. Dr. A. Rosenauer
Institute of Solid-State Physics
University of Bremen
Otto-Hahn-Allee 1
28359 Bremen (Germany)
[c] A. S. Pranti, Prof. Dr. W. Lang
Institute for Microsensors, -actuators and -systems (IMSAS)
University of Bremen
Otto-Hahn-Allee 1
28359 Bremen (Germany)
[d] Dr. S. Kunz
Südzucker AG
Central Department Research, Development, and Services (CRDS)
Wormser Strasse 11
67283 Obrigheim (Germany)

Supporting information for this article is available on the WWW under https://doi.org/10.1002/open.202000344

machined combustion devices is the high-power consumption due to high working temperatures (about 400 °C). Furthermore, these sensors have an unfavorably long response time of several minutes, and MOS-based sensors defy continuous operation because they require recovery after hydrogen loading.[3,7] All these issues severely restrict the application of present-day sensors for fast and reliable detection of hydrogen gas in mobile safety or medical devices.[3,5–8]

As an alternative approach with promising performance, our group has recently presented micro-technology-based catalytic gas sensors with nano-structured networks of organic ligand-linked Pt nanoparticles (NPs) as hydrogen combustion catalysts. The general working principle of catalytic combustion gas sensors is the detection of reaction heat produced by the exothermic oxidation of a combustible gas (e.g. hydrogen or volatile organic compounds) at the catalyst.[3,7–9]

Due to their high surface-to-volume ratio, NPs provide a high density of adsorption sites of varying coordination (terrace, edge or corner sites) which are potentially catalytically active.[10,11] Unfortunately, the tendency towards minimization of surface energy renders NPs prone to sintering if they lack stabilization.[12,13] Morsbach et al. demonstrated that the activity of pure Pt NP ensembles for catalytic hydrogen oxidation decreased rapidly due to reduction of their total surface area.[9,11] In order to prevent NP catalysts from sintering, these are typically supported on ample amount of inorganic support material (such as SiO_2, MgO, TiO_2 and Al_2O_3) which then accounts for 90–99 wt.% of the entire catalyst weight.[14–17] In case of catalytic hydrogen gas sensing, however, not only a high density of active sites but also a low heat capacity of the catalytic material is desired for high sensitivity and fast response of the sensor.[3]

Choi et al. demonstrated the use of a maximum of 10 wt.% Pt on Al_2O_3 as catalyst for hydrogen gas sensing. At an operation temperature of 100 °C, adding 1 vol.% of hydrogen to air led to an increase of the catalyst temperature by 47.3 °C and a thermoelectric detector signal of about 0.33 mV/°C. From the data presented in Reference [17] a rather slow response time (time passing until the sensor reaches 90% of the maximum thermoelectric signal after admission of hydrogen) of approx. 1 minute can be estimated which is presumably due to the high amount of catalytically inactive, inorganic support material.

Networks of organic ligand-linked Pt nanoparticles, in contrast, exhibit a high weight fraction of the catalytically active metal, a high local confinement of the catalyst, and a comparatively low heat capacity for a given metal load. As Morsbach et al. demonstrated, functionalization of the Pt NPs with bifunctional organic ligands may result in cross-linked Pt NP networks with inter-particle distances on the order of NP diameters, yielding a material with high density of NPs consisting of 70 wt.% Pt and exhibiting a porous morphology.[11]

With this type of catalyst (Pt NPs linked with p-phenylene diamine) a micro-fabricated, thermopile-based sensor chip demonstrated, at an operation temperature of 110 °C, an increase of temperature by 47.8 °C upon admission of 1 vol.% H_2 in synthetic air, comparable to Choi et al.,[17] but a larger thermoelectric signal of 4.6 mV/°C and, in particular, a much faster response time of 150 ms.[3]

Besides sensitivity and response time, stability of the catalyst under catalytic conditions is another basic requirement for hydrogen gas sensing. While Pt NPs functionalized with monofunctional ligands are only stabilized by steric effects and NPs can still sinter under catalytic conditions, bifunctional ligands can link neighboring Pt NPs by chemical bonds. Such interconnects within the cross-linked Pt NP networks should enhance their stability during catalytic hydrogen oxidation by keeping the NPs on distance.[9]

In previous studies with only a small selection of different bifunctional ligands, best results were achieved using p-phenylene diamine (PDA)-linked Pt NPs, which demonstrated high sensitivity and long-term stability up to 25 hours in catalytic hydrogen oxidation. It was assumed that the chemical stability as well as the rigid structure of the phenyl ring is advantageous in this regard.[9,11]

The choice of ligands is, on the one hand, crucial for the chemical and thermal stability of the NP network. It will, on the other hand, affect the Pt NP distances within the ligand-linked network, its pore size and steric accessibility of Pt surface sites. One may conceive that selectivity towards hydrogen combustion could be tailored by excluding larger volatile organic compounds (VOCs) or that a pronounced macro- and mesoporous network structure could facilitate dissipation of the water formed by hydrogen oxidation and result in higher activity and allow for lower operating temperatures. In order to expand the materials variety and elucidate if the catalyst properties can be tuned in a rational manner, we have synthesized and characterized Pt NP networks linked by 5 different bifunctional amines as ligands. In the following, we present the design of four new nanostructured materials by ligand-linking of the same Pt NP building block with three aromatic ligands (for a rigid backbone) of varying length or sterical demand and one cycloaliphatic (i.e., non-aromatic) ligand, referencing their properties, in particular their stability, to the yet best ligand (PDA). In addition, we report for the first time studies on the morphology of ligand-linked NPs network films from the nano- to the micrometer range and demonstrate how their mesostructure varies in dependence of the time allowed for ligand-linking during synthesis.

Experimental Section

Materials Synthesis

Chemicals

For synthesis of the ligand-linked Pt NP networks, $H_2PtCl_6{*}xH_2O$ (ChemPur, Pt-wt.% 40.07), ethylene glycol (VWR, 99.7%), ethanol (VWR, 99.9%), acetone (VWR, 100.0%), cyclohexanone (VWR, 100.0%), hydrochloric acid (CHEMSOLUTE), sodium hydroxide (VWR, 99.3%), p-phenylenediamine (PDA) (Alfa Aesar, 97.0%), benzidine (BEN) (Sigma-Aldrich, 98.0%), 4,4''-diamino-p-terphenyl (DATER) (TCI Europe, 98.0%), 1,5-diaminonaphthalene (DAN) (TCI Europe,

98.0%), and trans-1,4-diaminocyclohexane (DACH) (TCI Europe, 98.0%) were used as purchased.

Synthesis of Surfactant-Free Pt Nanoparticles Dispersed in Cyclohexanone

The synthesis of Pt NPs was carried out in alkaline ethylene glycol (EG) without adding any stabilizing polymers, according to a method first reported by Wang et al.[18] and later modified by our group.[11] For this polyol process 0.500 g of H_2PtCl_6*xH_2O was dissolved in 25 ml ethylene glycol (EG) whereto 0.5 M NaOH dissolved in another 25 mL ethylene glycol were added under stirring. Thereby, a clear, yellow precursor solution with a nominal Pt concentration of 4.0 g/L (20.5 mM) was obtained. Upon heating this solution for 1.5 hours to 160 °C using a pre-heated oil bath, the solution turned black after 5 minutes of heating which indicated the formation of a Pt colloid suspension. After completion of the synthesis, 'surfactant-free' Pt NPs were obtained, meaning that they were only stabilized by weak ligands (CO and OH^-)[11,19] and the solvent.

Before any linking of Pt NPs with bifunctional ligands, the as-prepared surfactant-free Pt NPs were precipitated with HCl and transferred to a more suitable solvent (mono alcohol or ketone with lower boiling point) by redispersing the precipitate. More specifically, for precipitation, 2 vol.-equivalents of 1 M aqueous HCl solution were added to 3 ml of Pt colloid and thoroughly mixed by shaking. The suspension was centrifuged for 10 minutes and the supernatant solution was carefully removed. The precipitated NPs were washed with 5 mL of 1 M aqueous HCl solution and centrifuged again. After removing the supernatant solution, the precipitated Pt NPs were redispersed in 500 μL of cyclohexanone to obtain a black colloid dispersion of 24 g/L Pt (123 mM) without any precipitate. Since HCl solution does not mix with cyclohexanone, a separation of residues of the aqueous phase and the organic phase with Pt NPs occurred. To get rid of the aqueous phase, the Pt colloid was carefully transferred into a clean bottle using a pipette.

After this procedure, almost all synthetic residues were removed[11] and any $OH\leftarrow^-$ ions were neutralized and removed from the NP surface. Consequently, the surfactant-free Pt NPs were only stabilized by the solvent and CO at the NP surface which facilitates any subsequent functionalization. However, since the removed OH^- ions acted as strong electrostatic stabilizers, the Pt colloids in cyclohexanone were only stable for a few hours. It should be noted that, in contrast, as-prepared Pt NPs in alkaline EG did not show any precipitation even after months of storage.

At this point it should also be noted that even with highest diligence, slight losses during the afore-mentioned, manual preparation steps cannot be avoided and lead to a somewhat reduced Pt concentration of the redispersed NP colloid (for numbers see section 2.3.4). Nevertheless, due to the fact that ligand-linked Pt NP networks were prepared in two independent, consecutive synthesis steps (particle synthesis and cross-linking), the network formation is detached from Pt NP synthesis so that material properties may be altered by selectively varying the ligand molecules while keeping the Pt NP building block the same.

Preparation of Ligand-Linked Pt NPs

All ligand-linking of Pt NPs was carried out with freshly redispersed surfactant-free Pt NPs by mixing a fresh solution of a bifunctional amine of choice in cyclohexanone with Pt NP colloid using an equimolar ratio of ligand and Pt. Figure 1 depicts skeletal formulae of the ligand molecules employed in this work. In general, two different methods were used for mixing amine ligand solution and NP colloid, depending on the amount of ligand-linked Pt NP sample needed for different characterization techniques.

Samples prepared for scanning electron microscopy (SEM) or for Fourier transform infrared spectroscopy (FTIR) were based on a small volume of ligand solution that was deposited as a small droplet on a die of clean Si wafer by an Eppendorf pipette. Afterwards a similar amount of Pt NP colloid was administered directly into the ligand solution droplet, and the mixture was then let dry at air in a fume hood. Since ligand-linking of NPs should only proceed as long as ligand is dissolved and Pt NPs are dispersed, the formation of the cross-linked material is expected to stop when the solvent has completely evaporated from the Si wafer. The time for complete solvent evaporation was visually estimated as approximately 30 min when samples were placed in the fume hood without any cover and as 8 hours maximum when they were placed under a watch glass cover to reduce solvent evaporation. To investigate influences of cross-linking duration on the morphology of the resulting material, these two drying variations, denoted 'regular drying' and 'prolonged drying' in the following, were employed for comparison.

In more detail, 75 μL (for FTIR) or 10 μL (for SEM) of 123 mM solutions of PDA, BEN, DACH or DAN or 112.5 μL (for FTIR) or 15 μL (for SEM) of 82 mM DATER-solution in cyclohexanone were used together with 75 μL (for FTIR) or 10 μL (for SEM) of Pt NPs redispersed in cyclohexanone (24 g/L, 123 mM). The formation of ligand-linked NPs upon drying was indicated by precipitation of an insoluble black solid. After complete evaporation of cyclohexanone, all samples were washed by thorough rinsing with acetone in order to remove any excess of ligands. The samples were then dried in a desiccator. For reference, FTIR spectra of the neat components, the pure Pt NP colloid as well as the solution of pure ligand in cyclohexanone were administered onto a Si wafer and let dry in a desiccator.

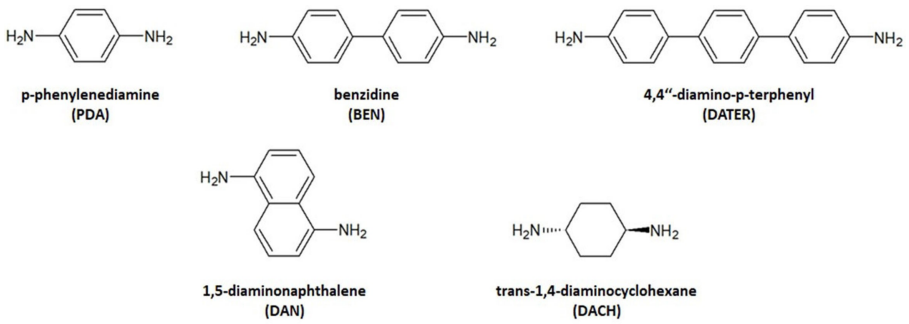

Figure 1. Compounds used as ligands.

For transmission electron microscopy (TEM), ligand-linked Pt NPs were prepared in the same way as described above using TEM grids (carbon-coated Cu-mesh) instead of Si wafer dies as support. Only 5 μL of both, the Pt NPs redispersed in cyclohexanone and the ligand solution, which were diluted with cyclohexanone to 2.4 g/L and 12.3 mM, respectively, were used. After solvent evaporation, all cross-linked samples for TEM were washed by rinsing with acetone and subsequently dried in a desiccator. For TEM investigations of pure Pt NPs, two droplets of Pt colloid (24 g/L) in cyclohexanone were diluted with 1 mL acetone. Three droplets of this diluted colloid were administered onto a TEM grid and let dry at air after each single drop.

For elemental analysis (EA), atom absorption spectroscopy (AAS), and thermogravimetric analysis (TGA) larger sample quantities were required. Therefore, larger amounts of ligand solution and NP colloid were mixed in centrifuge tubes. Here, evaporation of the solvent was prevented by sealing the centrifuge tubes and the reaction time between ligand and Pt NP could be easily adjusted by varying the duration of stirring and centrifuging. In more detail, 400 μL of 123 mM solution of PDA, BEN, DACH or DAN or 600 μL of 82 mM solution of DATER in cyclohexanone were given into a centrifuge tube with a small magnetic stirring bar. To this solution 400 μL of Pt NPs redispersed in cyclohexanone (Pt: 24 g/L, 123 mM) were added, resulting in an equimolar ratio of Pt to ligand. All centrifuge tubes were covered by a lid and stirred either for 30 minutes or for 24 hours. After 24 hours, any cross-linking reactions were expected to have completed. A reaction time of 30 minutes was chosen to produce samples to be compared to networks prepared on Si wafer dies which were let dry at air for 30 minutes (regular drying), as described above. After stirring, the content of the tube was centrifuged for 10 minutes and the supernatant solution was removed. The precipitated ligand-linked Pt NPs were washed two times with 5 mL of acetone and centrifuged again. After drying in a desiccator, fine black powders were obtained which were weighted and used for further analytics.

It should be noted that in previous work ethanol instead of cyclohexanone was used as organic solvent for redispersion of the Pt NPs and dissolution of the ligands.[9,11] The first, eminent drawback of the usage of ethanol as solvent is that DATER and DAN are not soluble in ethanol. Furthermore, after centrifuging pure Pt NPs (without any ligand) redispersed in ethanol or cyclohexanone, we found that the surfactant-free Pt NPs showed a significantly more stable suspension in cyclohexanone (see section 2.3.4). Also, cyclohexanone showed a lower evaporation rate compared to ethanol which has advantages for the dispensing process by which ligand-linked Pt NP network layers are produced on micro-fabricated sensor chips for catalytic gas sensing.

Materials Characterization

The sample structure and morphology were characterized by electron microscopy (TEM, SEM) and FTIR, their composition and thermal stability were analyzed by EA, AAS, and TGA-DSC.

FTIR spectra were recorded with a Bruker Vertex 80v spectrometer in transmission mode at a resolution of 4 cm^{-1}. For a higher quality of IR spectra, the sample compartment of the spectrometer was evacuated to a base pressure below 3 mbar. The software OPUS 6.5 was used for recording and evaluating IR absorption spectra. For each measurement, 128 scans were averaged to improve the signal-to-noise ratio. As background, the average of 128 spectra obtained for a clean Si wafer were subtracted. The IR spectra of the samples often exhibited a declining transmission for increasing wave numbers probably caused by scattering of IR light at the sample surface roughened by the deposited Pt NP network film.[11] In order to compensate for that, an automatic baseline correction was employed which left the spectral details unaltered.

For TEM and Scanning TEM tomography, a FEI Tecnai S TWIN microscope operated at 200 kV acceleration voltage and a non-probe corrected Titan 80-300ST system operated at 300 kV were used. Tilt series for tomography consisting of 99 images in the angle range from $-70°$ to $+70°$ were acquired applying the Xplore3d acquisition software with the Titan microscope in the Scanning TEM mode using a Fischione Model 2020 tomography sample holder and a Fischione high-angle annular dark field detector Model 3000 for Z contrast imaging. This technique provides a monotonously increasing behavior of the image intensity with specimen thickness and therefore fulfills the requirements for tomographic reconstruction. The tilt series were aligned and reconstructed using the backprojection algorithm as implemented in the IMOD software package.[20] Further evaluation of the reconstructed density were carried out within self-written MATLAB scripts.

SEM images were acquired with a Zeiss Auriga 40 field emission microscope equipped with a Gemini column, using the Smart-SEM V06.00 software. It was operated at a primary electron energy of 3 keV and with an aperture of 30 μm. For magnifications below 10000, a SE2 detector (Everhart-Thornley) was used whereas for higher magnifications an InLens detector (patented by Zeiss) was employed.

The Pt content in ligand-linked Pt NP was determined using a fast-sequential atomic absorption spectrometer (Varian AA 280 FS). For determination of C, H, and N contents of these samples an elemental analyzer (HEKA tech Euro EA) with chromatographic separation and a thermal conductivity detector (TCD) were used.

Combined TGA and DSC experiments were performed in a Mettler Toledo TGA/DSC 3+STARe System in 20 mL/min synthetic air flow as purge gas. A temperature ramp from 25 to 1000 °C at a rate of 10 °C/min was applied which left only Pt as remaining species. For each experiment around 5 to 8 mg of sample were used, data were always averaged over 2–3 individual experiments at identical conditions, and the STARe Evaluation Software 14.00 was employed for recording and evaluating the data.

2. Results and Discussion

Given the high stability and sensitivity that p-phenylene diamine (PDA)-linked Pt NP network catalysts demonstrated in previous hydrogen sensor tests,[11] the choice of ligands for this work was restricted to bifunctional organic molecules with a sterically rigid and chemically stable, preferentially aromatic backbone. In order to investigate how material properties such as interparticle distance and morphology which may affect the accessibility of gaseous reactants by e.g. different pore sizes can be tuned deliberately while maintaining thermal and chemical stability of the network, the aromatic ligands benzidine (BEN), 4,4''-diamino-p-terphenyl (DATER), and 1,5-diaminonapththalene (DAN) were chosen. While PDA, BEN and DATER represent a direct variation of ligand length (see Figure 1), DAN is expected to put higher steric demand on the formation of the NP-network and its penetrability by gaseous reactants due to the more compact shape of DAN as compared to BEN. In addition, the cycloaliphatic ligand trans-1,4-diamino-cyclohexane (DACH) was investigated as a non-aromatic but

cyclic counterpart to PDA for ligand-linking of Pt NPs to identify supposed benefits of aromatic backbones for chemical and thermal stability.[9]

2.1. Transmission Electron Microscopy

To obtain high-resolution structural information on the ligand-linked Pt NP networks, TEM studies were carried out. These revealed randomly distributed particles at varying distances and with a narrow size distribution with an average diameter of 1.5 nm ($\pm$0.3 nm) for surfactant-free Pt NPs redispersed in cyclohexanone (see Figure S1 in the Supporting Information for TEM micrograph). In contrast, after functionalization and cross-linking of Pt NPs with bifunctional ligands, indications for dense, three-dimensional Pt NP arrays were found in TEM (the organic ligands could not be resolved). As an example, Figure 2 depicts PDA-crosslinked Pt NPs. TEM images of the other NP networks can be found in the Supporting Information (Figure S2).

The average size of the individual particles within these arrays appeared unaltered after ligand-linking. It was impractical to accurately determine inter-particle distances within the NP arrays from single TEM pictures because they represent only a two-dimensional projection of potentially three-dimensional Pt NP networks. Hence, STEM tomography was employed close to the resolution limit for a non-probe corrected STEM in order to obtain a three-dimensional map of the density of the NP array structure (tomogram). Reliable estimates on average inter-particle distances were obtained from these tomograms in the following manner:

To identify all NP positions within the imaged array, an iterative procedure was employed. As first step of each iteration, the absolute maximum of density of the tomogram was searched and its position was determined. To refine this presumed particle position, the center of mass (COM) within a radius of $r_0 = 0.7$ nm around was calculated and taken as refined particle center position (corresponding to about the average Pt NP radius as determined from TEM images of pure, surfactant-free Pt NPs). In a second step of each iteration, the density was set to zero in the tomogram data within a sphere of radius r_0 around the identified particle center position (i.e., figuratively the identified particle was removed from the data). This two-step procedure was then repeatedly performed, producing a set of particle center positions r_i, until the density maximum of the remaining tomogram data was below a threshold value I_{th} (see the Supporting Information for information on how I_{th} was chosen).

Using the obtained set of particle center positions r_i, the distances between each particle i and all other positions r_j was calculated giving a distance matrix d'_{ji} which was subsequently sorted in an ascending manner. This matrix d_{ni} contained the distances between the center position of particle *i* and that of its *n*-th next neighbors. By averaging this matrix along the second dimension, mean distances d_n of the *n*-th next neighbors could be calculated.

Figure 3a) shows these mean distances depending on n for 5 different ligand-linked Pt NP arrays. A clear trend, comparing the different ligands used, can be only found for n larger than 2. The trend is impeded for small particle distances probably due to coalescence of some NPs which was visible in the TEM data. Therefore, in order to obtain a more reliable estimate of average nearest-neighbor inter-particle distances, a different approach was chosen: For a sphere of given radius R and volume $V = 4\pi R^3/3$ around the center of mass of an entire Pt NP array, the number N of particle positions within that sphere was determined from the set of particle center positions r_i, and the average volume per particle V/N was calculated. Assuming an average coordination number of 6 as in a cubic lattice, the average inter-particle distance (surface-to-surface) can be estimated as $\delta = (V/N)^{1/3} - 2r_0$. Figure 3b) shows δ depending on R for the 5 different ligand-linked Pt NP networks. While uncertainties are relatively large for R below 6 nm, particle densities on the borders of the networks differed strongly from the center of the arrays, leading to deviations for R larger than 10 nm. Therefore, as an estimate for inter-particle distances within the networks, Table 1 presents averages of δ over the range of R from 6 to 10 nm.

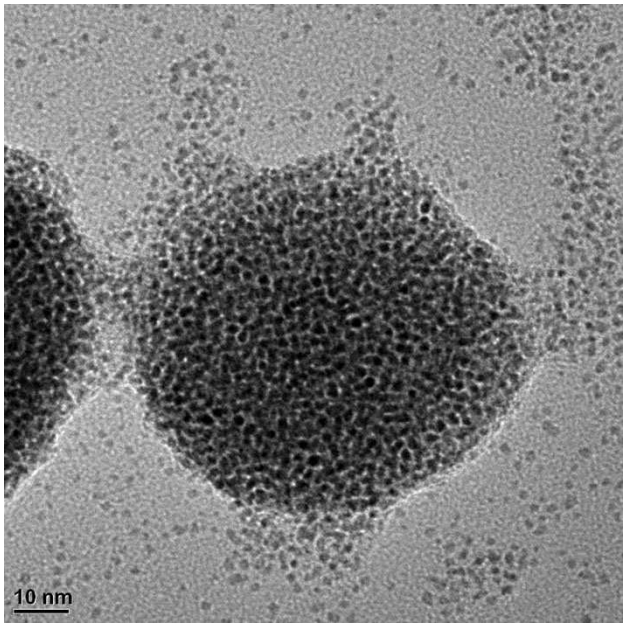

Figure 2. TEM of Pt-PDA.

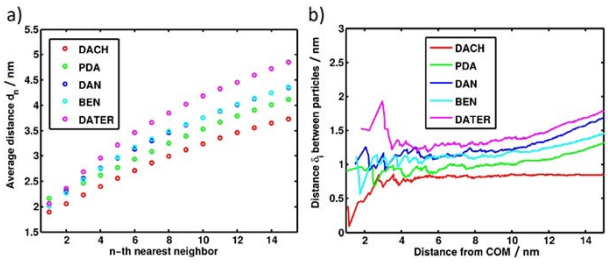

Figure 3. (a) Average distance between the center positions of Pt NPs and their n-th nearest neighbors as function of n, (b) measured inter-particle distance δ_i (surface-to-surface) as function of the particle distance from the center of mass (COM).

Table 1. Theoretical lengths of PtNP-ligand-PtNP units and average inter-particle distances (δ) estimated from TEM tomography (assuming an average NP coordination of 6). See text for details.

type	Length[a] of Pt–N-[ring system]-N-Pt	TEM tomography: Particle distance[b]
Pt-PDA	0.8–0.9 nm	0.8 nm (±0.1 nm)
Pt-BEN	1.2–1.3 nm	1.0 nm (±0.1 nm)
Pt-DATER	1.6–1.7 nm	1.4 nm (±0.1 nm)
Pt-DAN	0.8–1.0 nm	1.0 nm (±0.1 nm)
Pt-DACH	0.7–0.8 nm	0.7 nm (±0.1 nm)

[a] Given as range between minimum and maximum estimate.
[b] Standard deviation in brackets.

Therein, the inter-particle distances of all five ligand-linked NP networks calculated from TEM tomography data are compared to values expected from estimates based on regular bond lengths (C–C, C–N and N–Pt) and bond angles present in (Pt–N-[ring system]-N–Pt)-type structures.[21–23] Sheng et al. calculated 4 different adsorption modes of aniline adsorbed on Pt(111) surfaces. In two of those aniline interacts via the aromatic rings with the Pt and lies flat on the surface, while in others it binds via the nitrogen to the Pt surface whereby the aromatic ring appears angled to the surface and can exhibit two orientations.[22] Possibly, the less space-demanding adsorption of the ligand by the nitrogen is favored due to the competing coadsorption of CO on Pt NPs. Furthermore, Huang et al. reported a 31° tilt angle of aniline adsorbed on Pt(111) with respect to the surface.[24] One may imagine that the two Pt–N bonds from bifunctional amine to Pt NPs can be oriented in opposite directions giving the longest possible distance between the linked NPs or vice versa and everything in between. Taking these aspects into account, estimates for the minimum and maximum distances of nearest-neighbor NPs in the cross-linked networks were calculated (Table 1).

Overall, the experimental trend reflects very well the nominal lengths of the ligand structures. PDA, BEN and DATER, e.g., represent aromatic bifunctional amines with one, two and three rings in a row, respectively, and the experimental findings for the inter-particle distances in the Pt NP networks show a variation according to that order.

Also, DACH and PDA have both one six-membered ring (cyclohexane and benzene ring, respectively) in their structure, and we find, within errors, a quantitatively perfect match between the isolated ligand length and the inter-particle distance in the corresponding ligand-linked Pt NP networks. Similar to BEN, DAN has two benzene rings in its structure, but in contrast to BEN, the rings in DAN are bridged by two C atoms and the two amino groups in DAN (in 1–5 position) should exhibit a smaller distance than those in BEN so that inter-particle distances in Pt-DAN are expected roughly between those of Pt-PDA and Pt-BEN. However, by tomography we find the same δ for both, Pt-DAN and Pt-BEN.

In summary, the particle distances estimated from TEM tomography data for Pt-PDA, Pt-DACH and Pt-DAN match qualitatively very well with the theoretical expectations while the experimental inter-particle distance estimates for Pt-BEN and Pt-DATER appear compressed by about 0.2 nm. This slight deviation may be due to a denser packing of NPs in these networks, which would compromise the assumption of a fixed coordination number on which the experimental estimate is based. It should be noted that Fourier transformation of the tomograms did not provide any indication for a denser ordering of NPs in the Pt-BEN and Pt-DATER networks. Overall, however, the TEM experiments confirmed that inter-particle distances in ligand-linked NP networks could be varied and, to a large degree, deliberately tuned by the ligand used for the cross-linking.

2.2. Transmission Infrared Spectroscopy

The organic ligands which supposedly act as links and spacers between adjacent Pt NPs within the network could not be imaged, neither by TEM nor by STEM. To demonstrate their presence in the material and to elucidate how they bind to the Pt surface and whether they keep their molecular structure, FTIR spectra of pure Pt NPs, pure ligands and ligand-linked Pt NPs were recorded and compared. All samples for FTIR spectroscopy were prepared by deposition of ligand solution and Pt colloid on a Si wafer (cf. experimental section).

FTIR spectra of pure Pt NPs (Figure 4) exhibited a strong characteristic vibration band at 2055 cm^{-1} which can be attributed to the stretching mode ν(CO) of adsorbed carbon monoxide on Pt NPs, as reported before: Upon reduction of Pt^{+4} ions to Pt^0 during synthesis of the Pt NPs via the polyol process, ethylene glycol is oxidized. Besides other products such as oxalic acid, carbon monoxide is formed and remains as adsorbate on the Pt NP surface.[19] Apart from ν(CO), the FTIR spectrum of pure Pt–NP exhibited only minor features which point to small amounts of residues besides CO which were left over from the synthesis after washing the Pt NPs with HCl.

Our experimental value of 2055 cm^{-1} for ν(CO) on pure Pt NPs is blue-shifted compared to that of isolated CO molecules on Pt NP observed at 2020 cm^{-1} (singleton frequency), due to dipole-dipole coupling within dense arrays of CO.[19,25] Compared to density functional theory calculations for CO adsorbed on a clean Pt(111) surface by Gajdoš et al. who found ν(CO) at 2081 cm^{-1}, representing on-top adsorption at a quarter of a monolayer coverage,[26] however, our experimentally determined blue shift is less pronounced, indicating a lower coverage of CO on the NP surface, reducing the dipole-dipole coupling of the CO molecules.

The stretching mode of CO was also present in FTIR spectra of all Pt NP networks linked by aromatic ligands (PDA, BEN, DATER, DAN) (Figure 4). However, compared to pure Pt NP, the ν(CO) bands appeared with less intensity and were red-shifted from 2055 cm^{-1} by about 30 cm^{-1} (for details see Table 2) which is in good accordance with a previous report by Schrader et al.[19] The sheer presence of a ν(CO) vibration band for ligand-linked Pt NPs indicates ligand-free adsorption sites on the particles which, after removal of CO by thermal desorption or oxidation by air, are available, e.g., as catalytically active sites. The loss in intensity and, in particular, a red shift of the ν(CO)

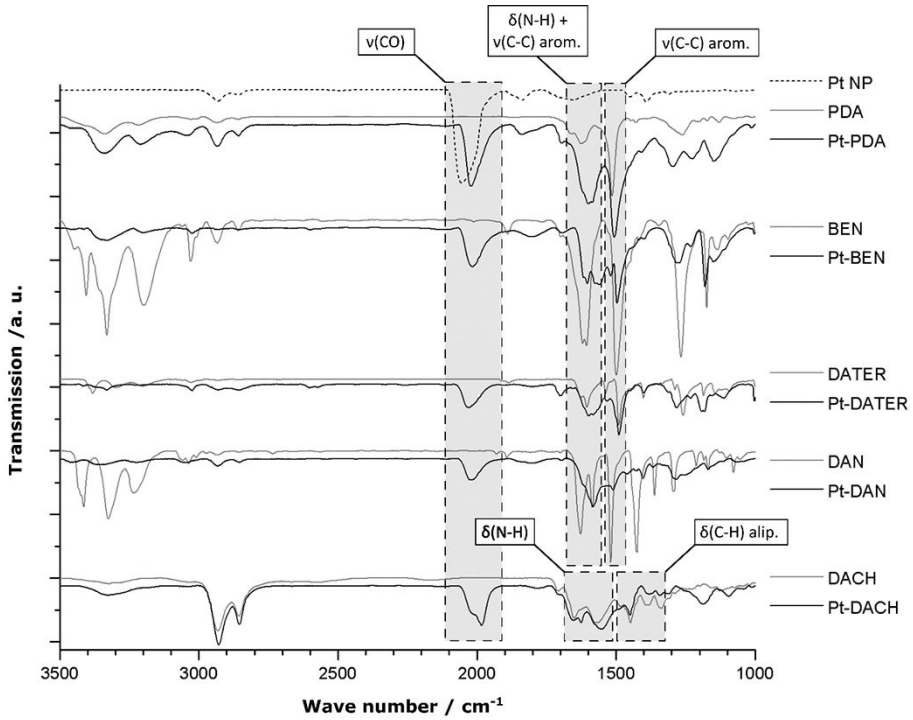

Figure 4. FTIR spectra of Pt NPs (dashes), bifunctional ligands (grey solid lines) and ligand-linked Pt NPs (black solid lines).

Table 2. Characteristic vibration bands of Pt NPs, aromatic ligands as well as Pt NP networks linked with aromatic ligands (red shifts of these bands with respect to the corresponding vibration in pure ligand or pure Pt NPs are given in brackets).

Sample Assignment	ν(CO) on top [cm^{-1}]	δ(N–H) scissor. [cm^{-1}]	ν(C–C) arom. [cm^{-1}]
Pt NP	2055	–	–
PDA	–	1624	1514
Pt-PDA	2023 (32)	1601 (23)	1507 (7)
BEN	–	1621	1607 1499
Pt-BEN	2019 (36)	1560 (61)	1606 (3) 1497 (2)
DATER	–	1627	1606 1537 1491
Pt-DATER	2033 (22)	1583 (44)	1600 (6) 1533 (4) 1490 (1)
DAN	–	1628	1587 1519
Pt-DAN	2026 (29)	1583 (45)	1583 (4) 1511 (8)

vibration compared to CO on plain Pt NPs is expected as result of dilution of adsorbed CO by the organic amine ligands which apparently almost eliminates dipole-dipole coupling between adsorbed CO molecules. (We note here that the ν(CO) vibration-related FTIR band disappeared after a few days when the samples were stored in air.)

FTIR of pure PDA, BEN, DAN, and DATER samples (Figure 4) showed signals characteristic for aromatic amines, assigned in the following according to References [27–29]. Bands observed in the region 1400–1000 cm^{-1} can be assigned to the δ(N–H) rocking and the ν(C–N) stretching mode as well as ν(C–C) stretching vibrations of the aromatic ligand. The spectral range 3400–3000 cm^{-1} can be related to the ν(N–H) stretching mode and ν(C–H) aromatic stretching vibrations. After the ligands were linked with Pt NPs (especially in the case of Pt-DAN), all these signals often showed low intensities and significant broadening (Figure 4) which rendered clear signal assignments difficult after ligand-linking.

In contrast, FTIR signals in the ranges of 1630–1620 cm^{-1} and 1610–1500 cm^{-1} which can be attributed to the scissoring vibration mode of the amino group (δ(N–H) scissoring) and to other stretching modes of aromatic carbon-carbon bonds (aromatic ν(C–C)), respectively, remained sharp and strong even after ligand-linking of the Pt NPs. Therefore, these vibrational bands were chosen to investigate how the respective bonds (N–H and C–C) within the ligands are affected by linking to Pt NPs. (It should be noted that for pure BEN and DATER, the δ(N–H) scissoring mode and the aromatic ν(C–C) vibration appeared within the 1630–1600 cm^{-1} range not perfectly separated but partially superimposed (Table 2).

For the δ(N–H) scissoring mode, a red-shift by 23–61 cm^{-1} was found after ligand-linking of Pt NPs with the bifunctional aromatic amines (Table 2). Wong et al. have reported such a red shift of δ(N-H) scissoring as indicator of coordinative bonding of the amino group in the case of the adsorption of cycloaliphatic amines on Germanium surfaces.[30] In our FTIR spectra, this red shift of δ(N–H) appears to be – in addition to the red shift of the ν(CO) vibration – a clear fingerprint of ligand-linked Pt NPs.

Since the C–C bonds of the aromatic rings are not expected to interact strongly with the Pt NPs surface within the network,

the aromatic ν(C–C) vibration of the pure ligands should not change significantly upon linking to Pt NPs.

In fact, while for BEN the initially superimposed ν(C–C) and δ(N–H) vibration modes were separated after ligand-linking, the corresponding vibration bands of Pt-DAN were superimposed, forming one broad signal after ligand-linking, in both cases due to a red shift of the δ(N–H) scissoring mode induced by the bond formation between the respective amine and Pt. The aromatic ν(C–C) stretching modes remained visible in the region of 1606–1490 cm^{-1} of the FTIR spectra for all aromatic ligand-linked Pt NPs and revealed only minor redshifts (by up to 8 cm^{-1}) as expected (Table 2).

Unexpectedly, signals from aliphatic compounds appeared occasionally at 2934 and 2862 cm^{-1} in IR spectra of Pt NP networks linked with aromatic ligands (Figure 4). These vibration bands can be related to residues of cyclohexanone, which were possibly encapsulated in the network during sample preparation.

As a non-aromatic alternative, the cycloaliphatic ligand DACH was tried for ligand-linking of Pt NPs and characterized in comparison with the aromatic structures. The FTIR spectra of Pt-DACH, pure DACH as well as pure Pt NPs are shown in Figure 4. In the wavenumber range expected for the stretching mode of CO adsorbed on cross-linked Pt NPs, two partially superimposed absorption bands at 1984 cm^{-1} and 2020 cm^{-1} can be found for Pt-DACH. The vibration band at 2020 cm^{-1}, which is red-shifted by 35 cm^{-1} with respect to CO adsorbed on pure Pt NP, is in good accordance with the FTIR signals for CO on PtNPs cross-linked by aromatic diamines. Also here, we ascribe the red-shift to a more diluted adsorption of CO on cross-linked Pt–NPs, lacking the amount of dipole-dipole coupling expected within a dense CO layer on pure Pt NPs.[19,25]

The origin of the signal at 1984 cm^{-1} is not obvious. It appears at lower wavenumbers even than the singleton frequency of CO adsorbed at on-top sites on Pt surfaces reported by Schrader et al.[19] Furthermore, DACH is not expected to exhibit IR absorption at around 2000 cm^{-1} and CO on bridge site and hollow site should show up in the significantly lower wavenumber range of 1850–1736 cm^{-1}.[26] Hence, the 1984 cm^{-1} signal may be related to a different effect. Kappers et al. reported that the relative amount of terrace, edge, and corner sites on Pt NPs has a significant influence on the vibrational band of CO. Low-coordinated adsorption sites (step edges or corners) led to lower CO stretching frequencies.[31] Since amino groups of DACH deviate by higher basicity (more pronounced lone electron pair on the nitrogen) from the aromatic ones, the preferred surface adsorption sites for CO on ligand-linked Pt NPs may well be different for DACH and, e.g., PDA. One may speculate that on Pt-DACH CO adsorbed at low-coordinated Pt sites is more abundant, leading to the pronounced band maximum at 1984 cm^{-1}.

Pure DACH showed, among others, ν(N–H), ν(C–H) and δ(C–H) as characteristic vibrational bands in FTIR (assigned according to References [30–33]). Our experimental FTIR spectrum of pure DACH also showed two strong vibration bands at 1567 and 1651 cm^{-1}. After DACH-linking of Pt NPs, three signals appeared at 1552, 1626, and 1652 cm^{-1}, i.e., the first band appeared to have shifted red by 15 cm^{-1} while the second appeared to have split into one band shifted red by 25 cm^{-1} and another without significant shift with respect to pure DACH. As mentioned above, such red-shifts can be correlated to coordinate bonding of the nitrogen as reported by Wong et al.[30] Therefore, we relate the signals at 1567 and 1651 cm^{-1} to the amino group of DACH.

In fact, Pažout et al. recorded and calculated IR spectra of cis-[Pt(DACH)I_2] and ascribed bands at 1658 and 1632 cm^{-1} to the deformation vibration δ(N–H) of the amine.[32] In addition, they found a strong signal at 1557 cm^{-1} which was not further discussed. Other investigations reported δ(N–H) scissoring related bands for similar Pt-DACH systems in the range of 1550–1605 cm^{-1} or 1609–1620 cm^{-1}.[30,33] Given the good agreement between our findings and the work of Pažout et al., we ascribe the FTIR signals observed in the range of 1622–1652 cm^{-1} to δ(N–H). While we cannot pinpoint the origin of the signal at 1552–1567 cm^{-1}, it is apparently also associated with the amino group of DACH. The strong component of the δ(N–H) signal at 1651 cm^{-1} which did not shift upon the reaction of DACH with Pt NPs may represent amino groups which are not linked to Pt and thereby indicates that the linking reaction with the bifunctional DACH probably remained partially incomplete. We note that the exclusive observation of a red-shifted δ(N–H) band for, e.g., PDA-linked Pt NPs is no unequivocal evidence that in that case all amino groups are bound to Pt NPs. In contrast to DACH, both amino groups of an aromatic amine, i.e., with conjugated C–C bonds, may exhibit resonance interactions which can lead to a single δ(N–H) band irrespective of both amino groups being in different chemical conditions.[30] Nevertheless, the degree of the red-shift may be affected by the fraction of free amino groups. However, the fact that we found only one δ(N–H) band with a significant red-shift compared to the pure ligands (in accordance with Wong et al.[30]) for PDA, BEN, DAN, and DATER after ligand-linking of Pt NPs indicates that most of the ligands were in similar bonding configurations. The stability of the ligand-linked networks to be demonstrated later corroborates the interpretation that a large fraction of the aromatic ligands were bound to Pt NPs via both of their amino groups. In addition to the amino group-related bands, FTIR of DACH-linked Pt NPs showed three δ(C–H) vibration modes at 1344, 1382 and 1451 cm^{-1} and a doublet at 2928 and 2855 cm^{-1} representing the ν(C–H) stretching mode. Only the vibrational bands at 1344 cm^{-1} and 2928 cm^{-1} revealed minor shifts with respect to pure DACH, the others were not affected by the linking reaction at all. Table 3 collects all relevant characteristic vibration bands of DACH and Pt-DACH.

In conclusion, our FTIR study confirms the presence and intactness of aromatic and aliphatic ligands in all samples of ligand-linked Pt NPs via the perseverance of characteristic vibrational bands of the ligands after the linking reaction with Pt NPs. Furthermore, IR spectroscopy reveals that interaction of the ligands with the surface of Pt NPs is dominated by the amino groups and indicates coordinate N bonding by a characteristic red-shift observed for signals of amino deformation vibrations. In addition, a red shift of the CO stretching

Table 3. Vibrational bands of CO and of DACH, as identified for pure DACH and for Pt NP networks linked with DACH. (Band shifts with respect to CO on pure Pt NPs or with respect to pure DACH given in brackets).

	ν(CO) on Top [cm^{-1}]	δ(N–H) scissor [cm^{-1}]	ν(C–H) alip. [cm^{-1}]	δ(C–H) alip. [cm^{-1}]
DACH	–	1651 1567	2931 2857	1448 1384 1337
Pt-DACH	2020 (−35) 1984 (−71)	1652 (+1) 1626 (−25) 1552 (−15)	2928 (−3) 2855 (−2)	1451 (+3) 1382 (−2) 1344 (+7)

vibration which can be interpreted as dilution of the adsorbed CO by the amine ligands corroborates that there is successful ligand-linking of Pt NPs.

Since vapors of VOCs (e.g. alcohols or hydrocarbons) can be present in the atmosphere, the systems were also investigated regarding the stability against organic solvents. Therefore, samples of Pt-PDA were stored in ethanol, acetone, cyclohexanone, and hexane for 24 hours and then probed by FTIR spectroscopy. Since water is formed by catalytic hydrogen oxidation, a FTIR spectrum was also recorded after 24-hour exposure to water. All these spectra for samples after exposure to organic solvents or water showed no significant change in signal positions and thereby demonstrated that the coordinative bonding of amines on Pt NP remained stable under these harsh conditions. (For FTIR spectra of PDA-linked Pt NPs after exposure to ethanol, acetone, cyclohexanone, hexane, and water see Figure S3 in the Supporting Information).

2.3. Composition of Ligand-Linked Pt NP and Related Thermal Properties

2.3.1. Composition by Elemental Analysis and Atomic Absorption Spectroscopy

Elemental analysis (EA) and atomic absorption spectroscopy (AAS) were applied to determine the composition of the ligand-linked Pt NP networks. In combination with information on the Pt NP shape and diameter, knowledge about the total content of Pt as catalytically active species is required to compare activities of different catalysts via turnover frequencies. A high Pt-to-ligand ratio within the network is expected to be beneficial for the response time and the sensitivity of the sensor chip. The stoichiometry of C, H, and N provides information on whether the structure of the organic ligands is maintained during formation of the ligand-linked Pt NP network.

Samples for EA and AAS were obtained after 24 hours of reaction time and prepared in centrifuge tubes as described in the experimental section. Table 4 displays the experimentally determined Pt fraction (in wt.%) for all samples analyzed. While Pt-PDA, Pt-BEN, Pt-DACH and Pt-DAN exhibited a Pt content of around 52–56 wt.%, Pt-DATER had a significantly lower Pt content of 44 wt.%. Overall, however, the amount of catalytically active metal in ligand-linked Pt NPs was high compared to Pt NPs conventionally supported on oxides (e.g., 1–10 wt.% Pt on Al_2O_3[16,17]). Since the chosen organic ligands have no oxygen in their chemical structure (Figure 1), only the contents of C, H, N can be related to them. The content of oxygen detected by EA could be related to CO on Pt or residual H_2O or cyclohexanone in the material.

Table 4 presents the contents of the elements C, H, N, Pt, and O in atom % as calculated from the raw data given in wt.% (see Table ST1 in the Supporting Information for the EA and AAS raw data). The atomic ratio of N:Pt is a measure for the number of ligands (each with 2 N atoms) per Pt atom. Based on a model presented by Mori et al. for quasi-spherical icosahedron-shaped Au NPs (also a face-centered cubic lattice),[34] we estimate the total number of Pt atoms in each Pt NP with an average diameter of (1.5 ± 0.3) nm as 55 atoms (2 shells) with 42 of them (76%) representing surface atoms. Thereby we obtain calculated numbers of ligands per Pt surface atoms in the range of 0.72–0.96 (Table 4). If one bifunctional ligand binds to two individual NPs and saturates one Pt surface atom on each NP, this value should be 0.5 at maximum. The discrepancy indicates that some of the bifunctional ligands probably bind only to one Pt NP or do not bind to Pt at all. In fact, the ligand-Pt network forms a macroporous material (as evidenced by SEM, see section 2.4) with a high outer surface area on which ligands will bind only to a single Pt NP. Also, ligands could be encapsulated inside of mesopores or -cavities of the material and therefore be bound to no Pt NP at all.

The atomic ratios N:C and N:H should represent the stoichiometry of the respective ligand involved. Table 5 shows the stoichiometries that were calculated from the atomic ratios N:C and N:H determined by EA, based on the assumption that all C, H, and N content represents diamine ligands (see values

Table 4. Data of AAS in wt.% and EA in Atom% of elements. Also shown are derived atomic and molecular ratios.

	Pt-PDA	Pt-BEN	Pt-DATER	Pt-DAN	Pt-DACH
AAS: wt.% Pt	52.98	52.31	43.81	55.33	55.56
Atom% C	35.97	43.07	46.38	40.31	27.91
Atom% H	37.69	37.21	38.76	35.00	48.16
Atom% N	7.30	5.10	3.93	6.29	6.91
Atom% Pt	4.99	4.67	3.20	5.48	4.74
Atom% O	14.06	9.95	7.73	12.92	12.29
Atomic ratio N:Pt	1.46	1.09	1.23	1.15	1.46
Number of ligands per Pt atom	0.73	0.55	0.62	0.57	0.73
Number of ligands per Pt surface atom	0.96	0.72	0.81	0.75	0.96

Table 5. Element stoichiometry of pure ligands (theoretical values are normalized to nitrogen of one molecule: No. of N = 2.0) and experimentally determined values in ligand-linked Pt NP (without compensation and compensated by CO).

		PDA	BEN	DATER	DAN	DACH
No. of C	theoretical	6	12	18	10	6
No. of H		8	12	16	10	14
No. of C	without compensation	9.9	16.9	23.6	12.8	8.1
No. of H		10.3	14.6	19.7	11.1	13.9
No. of C	compensated by CO	6.0	13.0	19.7	8.7	4.5

without compensation). At first sight, in particular the amount of carbon in the samples appears to be significantly higher than expected from the ligand structure (theoretical values). The ligand stoichiometries were then recalculated, taking into account the amount of oxygen present. Assuming that the entire oxygen represents CO and accounts for a respective amount of the carbon content, the residual C stoichiometry already matches fairly well the elemental stoichiometry of the ligands (table 5, values compensated by CO). The analysis could probably be further refined by taking also residual water and cyclohexanone into account for the balance of C, O and H content. Overall, the results indicate that the chemical structure of the ligands is well maintained after ligand-linking with Pt NPs.

2.3.2. Thermal Properties of Ligand-Linked Pt NPs.

Combined thermogravimetric analysis (TGA) and differential scanning calorimetry (DSC) were applied to investigate the thermal stability of ligand-linked Pt NP networks (a mass loss combined with the detection of heat generation within the sample was taken as indication of thermally induced decomposition reactions) and to determine the weight fraction of non-combustible residues (Pt, in our case). For that purpose, TGA was performed up to a temperature of 1000 °C (in synthetic air) at which only Pt should remain in the samples and all organic compounds should be completely decomposed and combusted. Thus, the total weight loss determined in our TGA experiments should represent ligands and other adsorbates such as CO and may be referenced to our AAS results. All samples for TGA-DSC were prepared in the same way as those for EA and AAS (see experimental section for details).

Figure 5 displays the TGA curves (total weight loss depending on temperature) and, as inset, the derivative of weight with respect to temperature (dm/dT) as well as DSC curves (reaction heat depending on temperature) of all ligand-linked Pt NP samples. The TGA curves reveal three to four qualitatively different desorption or decomposition processes until the sample masses remain constant at temperatures above ~450 °C for all materials:

The first mass loss process sets on at ~30 °C (we interpret mass losses larger than 3 μg/K as significant in our data) and is characterized by a relative minimum of dm/dT at around 50 °C and a total weight loss of 3 to 5 wt.% which is reached at temperatures in the range 130–185 °C, depending on the type of ligand. Since no significant heat generation was detected by DSC up to 130 °C temperature, we relate the weight loss to desorption of volatile residual gases or molecules such as CO, H_2O or cyclohexanone but not ligand decomposition reactions.

A major decomposition process is characterized by an absolute minimum of dm/dT in the range from 240–280 °C, depending on the type of ligand. For T > 130 °C, the minima of dm/dT coincide with maxima of the DSC signal and indicate the temperature at which the respective decomposition process

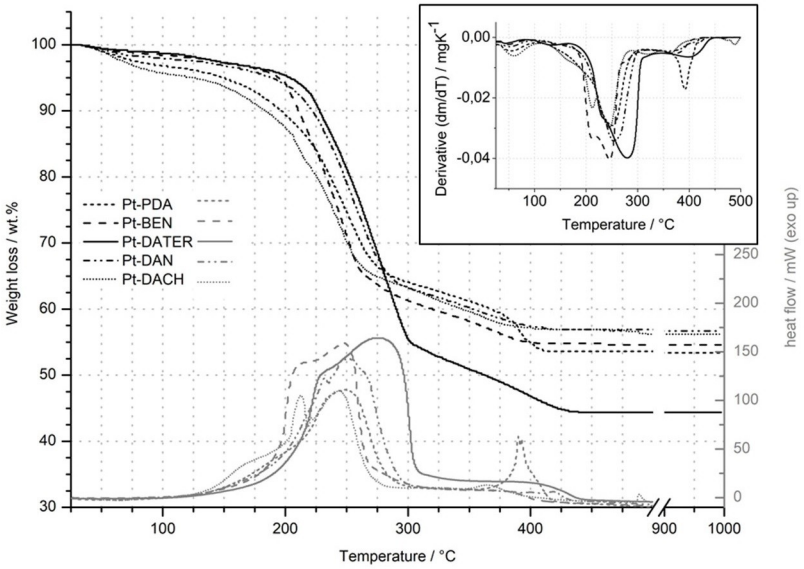

Figure 5. TGA curves (black) with the derivative dm/dT in the inset and DSC curves (grey) of all ligand-linked Pt NP.

has its highest turnover rate. The broad DSC curves, showing even an additional relative maximum in the temperature range 200–240 °C for Pt-BEN and Pt-DACH, indicate that there is a two-step process behind this major decomposition. For Pt-PDA and Pt-DACH, this process appears even to be preceded by another or to slowly start already at ~130 °C until massive weight loss sets on at approx. 200 °C, as for all the other materials. This major decomposition process leads to a weight loss in the range of 30–40 wt.% of the initial mass and ends at temperatures in the range 260–300 °C, indicated by a sudden change of the weight loss rate which levels off at a non-zero, but much lower, almost constant value.

The high-temperature decomposition (above 260–300 °C) leads to another total weight loss of about 10–14 wt.% of the initial mass for all samples and ends at temperatures in the range 420–450 °C, depending on the type of ligand, above which no further weight loss can be observed.

With respect to possible mechanisms behind the major decomposition processes we note the following: Huang et al. reported on possible reactions of aniline adsorbed on Pt(111) surfaces and discussed a splitting of the C–N bond at a temperature of ~180 °C behind the observed formation of benzene and ammonia (which they found depending on an admitted hydrogen atmosphere).[24] Based thereon, we speculate that also in the present study a route via splitting of the C–N bonds of the diamines may be behind the major decomposition process in the temperature range 200–280 °C noted in the TGA-DSC experiments.

Furthermore, it was reported that benzene as well as aniline adsorbed on Pt(111) surfaces can undergo dehydrogenation of the benzene ring, which forms hydrogen as well as a stoichiometric layer of C_6H_3 or C_2H at temperatures of ~150–290 °C, which decompose to graphitic carbon and hydrogen at more elevated temperature.[24,35] Therefore, we assume that the high-temperature decomposition observed in TGA/DSC represents combustion of remaining organic species to CO_2.

While TGA and DSC show the same trends, we base the following ranking of the thermal stability of the five different ligand-linked Pt NP networks on the DSC data because in contrast to TGA it unambiguously reveals exothermic combustion processes of the ligands. In order to have a comparative, well averaged, quantitative measure for an onset temperature of decomposition of all materials, the integrals from 25 to 450 °C of the DSC curves were evaluated (since the temperature was increased at a fixed rate of 10 °C/min, see experimental section, the integral value represents the total reaction heat). For each material, the temperature at which 2% of the respective total integral was attained was taken as onset temperature and led to values in the range 130–166 °C.

According to DSC, Pt-DATER exhibited the highest thermal stability with an onset decomposition temperature of 166 °C, followed by Pt-BEN and Pt-DAN with approx. 150 °C. Pt-PDA and Pt-DACH showed a lower initial decomposition temperature of approx. 130 °C. These materials should not be exposed to higher temperatures to maintain the intactness and therefore the activity of the catalysts. Apparently, thermal stability of ligand-linked Pt NPs is promoted by the number of (aromatic) rings within the ligand. Table ST2 in the Supporting Information contains all the detailed thermal properties (detailed weight losses of the three steps in TGA, temperature of minima and infliction points in the derivative dm/dT, temperature of initial decomposition as well as maxima of DSC curves). It should be noted that one may conceive thermal degradation processes of the ligands without desorption and weight loss. With our study, however, we cannot exclude that such degradation may already occur at temperatures below the onset of decomposition.

2.3.3. Correlation of Charred Residue by TGA and Pt Content by AAS

Finally, we comment on a comparison of the charred residue values determined at 1000 °C in wt.% of the TGA measurements with the Pt contents determined by AAS. In order to check their correlation, the charred residues by TGA of all materials were determined from 3 independent samples after 24 hours of reaction for verifying the reproducibility of this method. Accordingly, also, the product mass of each analyzed sample was determined. All product masses and charred residues of further samples (30 minutes of crosslinking) were determined 2 times. Table 6 summarizes the results. After 24 hours of crosslinking, Pt-PDA, Pt-BEN, Pt-DACH and Pt-DAN showed similar

Table 6. Charred residues, product masses and their share of Pt after 24 h and 30 min of reaction, the maximum scattering of the individual measurements is also given (±).

	Pt-PDA	Pt-BEN	Pt-DATER	Pt-DAN	Pt-DACH	Pt-PDA EtOH
crosslinking duration of 24 hours						
charred res. [wt.%]	53.2 ± 0.7	53.8 ± 1.3	44.3 ± 0.4	56.4 ± 1.5	55.9 ± 0.9	64.8 ± 0.4
product mass [mg]	15.7 ± 1.1	16.3 ± 1.1	19.0 ± 1.3	13.3 ± 0.3	14.6 ± 0.5	12.9 ± 0.2
Pt content [mg]	8.4	8.8	8.4	7.5	8.2	8.3
crosslinking duration of 30 minutes						
charred res. [wt.%]	74.7 ± 0.4	64.8 ± 0.0	58.8 ± 0.8	65.1 ± 0.4	65.8 ± 0.5	68.6 ± 0.7
product mass [mg]	3.1 ± 0.4	3.8 ± 0.2	9.3 ± 1.0	2.1 ± 0.2	12.3 ± 0.3	9.9 ± 1.8
Pt content [mg]	2.3	2.5	5.5	1.4	8.1	6.8
ratio of crosslinking duration of 30 min to 24 h						
Pt content [%]	27.4	28.4	65.5	18.7	98.8	81.9

charred residues of 53.2 wt.%, 53.8 wt.%, 55.9 wt.% and 56.4 wt.%, respectively. Pt-DATER exhibit a lower charred residue of 44.3 wt.%. These charred residues of TGA are in good accordance with the Pt content determined by AAS (Table 4). The TGA curves and the results of TGA (masses at 25 °C as well as at 1000 °C and the resulting wt.%) of all single measurements of all materials can be found in the Figures S4 and S5a–e, and Tables ST3 and ST4 in the Supporting Information.

2.3.4. On the Formation Rate of Ligand-Linked Pt NP

To gain insight into the formation rate of ligand-linked Pt NP networks and its dependence on the type of ligand or the solvent, samples prepared in centrifuge tubes at an allowance of 24 hours of reaction time (and even 96 hours in the case of Pt-PDA) were compared to samples which spent only 30 min in the centrifuge tubes. The duration of 30 min was chosen because it corresponds to the reaction time that we estimated as available to those samples which were prepared by codeposition of NP suspension and ligand solution onto Si supports (for SEM) before the solvent (cyclohexanone) had completely evaporated. To evaluate the total turnover, the absolute and relative Pt content of all washed product samples (insoluble ligand-linked Pt NPs) was determined by TGA via the charred residues. Besides the ligand, also the solvent was varied by using ethanol instead of cyclohexanone.

It can be assumed that if a ligand-linked NP network is growing, the resulting material becomes denser by lowering the distances of Pt NPs, causing NP network seeds to precipitate which may further grow. Besides the adsorption rates of the organic amines on Pt NPs, the formation rate of the insoluble material should depend on solubility limits of the resulting cross-linked product in the used solvent.

After 24 hours of reaction in the centrifuge tubes, the remaining supernatant solution was clear and showed the color of pure ligand solution (taking into account partial oxidation after storage) for all ligands and both, cyclohexanone and ethanol, as solvent. That indicated an excess of ligand and consumption of all Pt NPs by ligand-linking, i.e., after a reaction time of 24 hours the cross-linking of Pt NPs can be considered as completed.

In contrast, after 30 minutes of reaction the supernatant solutions were still dark brown in all cases except for Pt-DACH (to be discussed later), indicating that Pt NPs were still dispersed in the solvent and cross-linking of Pt NPs with the aromatic ligands had not yet completed.

Before commenting on the results of our TGA analysis quantitatively we note that always 400 μL of a Pt NP suspension nominally containing 24.0 g/L Pt in cyclohexanone or ethanol was used for sample preparation in the centrifuge tubes which should correspond to a total of 9.6 mg Pt. We found, however, that only 8.8 mg residue remained after complete drying of pure Pt colloid in cyclohexanone without any bifunctional ligand. The discrepancy may have been caused by losses during the preparation steps of the Pt NPs suspension as mentioned in the experimental section. As reference for ligand-linked Pt NP samples, we take 8.8 mg as total Pt content in the following.

After 24 hours of cross-linking, Pt amounts between 8.2–8.8 mg (93–100% of 8.8 mg) were found for Pt-PDA, Pt-BEN, Pt-DATER and Pt-DACH samples indicating that a high share of the Pt NPs were incorporated in the product. Pt-DAN samples exhibited a lower amount of 7.5 mg (85% of 8.8 mg) of Pt in the final material.

In one experiment, Pt-PDA was prepared with a reaction time of 96 hours, yielding a 15% higher total product mass (18.1 ± 0.3 mg) than that obtained after 24 hours of reaction. The charred residue (Pt content) corresponded to 8.4 mg Pt in the resulting material, similar to the residues obtained after 24 h. Obviously, although the formation of the NP network had completed by built-in of all available Pt into the product, the material can still bind more ligands.

The product masses obtained after 30 minutes of reaction were significantly lower (Table 6) than those obtained after 24 hours of cross-linking. Furthermore, the charred residues (Table 6) after 30 min of cross-linking were around 10–20 wt.% higher for all materials than after 24 h of cross-linking indicating a lower amount of bifunctional ligand in all materials after 30 minutes of reaction.

The amount of Pt incorporated in the product material after 30 minutes of reaction was 27%, 28%, and 66% of the applied Pt NPs for Pt-PDA, Pt-BEN, and Pt-DATER, resp., i.e., we found no clear trend for the formation rate depending on the number of aromatic rings in the ligand. The reason for the comparatively fast formation of Pt-DATER could be the low solubility of DATER observed already for the pure ligand. It may promote precipitation of the cross-linked material.

In Pt-DAN, only 19% of the total Pt NPs were incorporated in the product material after 30 min which, compared to Pt-BEN, the second aromatic ligand with two aromatic rings of our selection, indicated a slower formation rate for Pt-DAN. We assume that DAN has a sterically more demanding structure than BEN for network formation which may cause a lower formation rate of Pt-DAN.

In contrast to the aromatic ligands which all exhibit similar amino groups, the cycloaliphatic DACH has a chemically different amino group of higher basicity than the aromatic ones. We found that after 30 minutes of reaction, Pt-DACH incorporated 99% of the total Pt NPs in the product mass, i.e., the cross-linking reaction had already been completed. That is in contrast to the network formation from aromatic diamines, in particular from PDA which appears similar to DACH with respect to steric demands. Therefore, it appears likely that the higher amine basicity is at the origin of the higher network formation rate of DACH. Its lone electron pair should be more localized on the amino groups which may promote their adsorption on Pt and give rise to much faster formation of Pt-DACH in comparison to all aromatic ligand-linked systems.

To compare the ligand-linking of Pt NPs in cyclohexanone to the method of Morsbach et al., also ethanol was used as solvent. In these experiments, Pt-PDA in ethanol gave charred residues of 68.6 wt.% and 64.6 wt.% after 30 minutes and 24 hour of cross-linking, respectively, which were comparable

to the results of Morsbach et al. (approx. 70 wt.% Pt).[11] In particular, after 30 minutes of cross-linking in ethanol, the product network already contained 82% (6.8 mg) of the applied Pt NPs, (compared to 2.3 mg in cyclohexanone), and after 24 hours, Pt-PDA in ethanol contained 8.3 mg Pt, i.e., 94% of the applied Pt NPs (see Figure S6a–c and Table ST5 for original data in the Supporting Information).

The relatively fast product formation in ethanol may be related to our observation that pure Pt NPs redispersed in ethanol appeared less stable than in cyclohexanone: when pure Pt NPs in ethanol were stirred in centrifuge tubes under similar conditions, approx. 1/3 of these Pt NPs were already precipitated after 30 min, i.e., even without adding any bifunctional ligands. In contrast, pure Pt NPs redispersed in cyclohexanone under the same conditions did not yield any measurable precipitate after 24 hours. The relatively high fraction of Pt in the product obtained after 24 h of reaction in ethanol (68.6 wt.%) compared to that obtained in cyclohexanone (53.3 wt.%) indicates that NPs in ethanol may have aggregated or partially sintered and thereby impede complete functionalization with bifunctional ligands. Therefore, ethanol appears less suitable than cyclohexanone as a solvent for proper ligand-linking of Pt NPs.

2.4. Morphology

The morphology of a solid, heterogeneous catalyst is crucial for its performance on a length scale ranging from molecular dimensions up to the mean free path of the reactants. Besides the microporosity of the ligand-linked Pt NP networks, also macro- and mesopores are expected to be relevant for access of the reactant molecules to catalytic sites as well as for releasing product molecules from the catalyst. Therefore, scanning electron microscopy (SEM) was employed to characterize the structure of ligand-linked Pt NP networks deposited on Si wafer dies and to elucidate, how their macro- and mesoporosity may be tuned by the choice of ligand or the variation of reaction parameters, in particular the time allowed for ligand-linking.

2.4.1. Cross-Linking of Pt NP with PDA Using Different Drying Procedures

The reaction time of cross-linking PDA and Pt NPs was varied by procedures described in the experimental section, denoted 'regular drying' and 'prolonged drying', respectively. SEM pictures of pure Pt NPs (shown in Figure S7 in the Supporting Information) revealed a non-porous dense layer of Pt NPs with some aggregates on top. Neither macro- nor mesoporous structures were visible on the surface as well as in cracks at higher magnification. Since pure NPs lack any kind of stabilization, they are expected to sinter at elevated temperatures (catalytic conditions) and quickly form larger Pt structures.[12,13] The concomitant loss of surface area was regarded as origin of a rapid decay of catalytic activity reported by Morsbach et al.[9,11]

In contrast, SEM of Pt-PDA prepared by 'regular drying' of Pt NPs and ligand solution codeposited on Si wafer showed a flat and partially dense surface layer with μm wide cracks (Figure 6A). At higher magnification (Figure 6B), within the cracks, a mesoporous structure (pore dimensions of several 10 to 100 nm) became visible, hidden underneath the dense surface layer and in strong contrast to the dense layer of pure Pt NPs.

The heterogeneous nature of the morphology indicates that the cross-linking reaction had not completed after evaporation of the solvent, leading presumably to a precipitate of unlinked Pt NPs (and PDA) on top of the ligand-linked network structure. In fact, as shown in section 2.3.4, experiments with larger batches synthesized in centrifuge tubes indicated that a reaction time of 30 min (corresponding to the estimated reaction time of 'regular drying') was insufficient to incorporate all ligands from the solution into the PDA-Pt NP network.

Figure 6C and D shows SEM samples of Pt-PDA prepared by 'prolonged drying' on a Si wafer revealing a meso- and macroporous structure built up by spherules (with diameters from few to several 100 nm) which is significantly different from the morphology obtained for 'regular drying'. This is probably a consequence of the elongation of the reaction time which should allow for better cross-linking of the Pt NPs by incorporation of a higher share of ligands, as indicated by the evaluation of the reaction time-dependence of charred residues of cross-linked material prepared in centrifuge tubes presented in section 2.3.4.

Apart from the reaction time, also the solvent in which samples of Pt-PDA were prepared, was varied from cyclohexanone to ethanol for comparison in separate experiments. As pointed out in section 2.3.4, product masses of PDA-linked

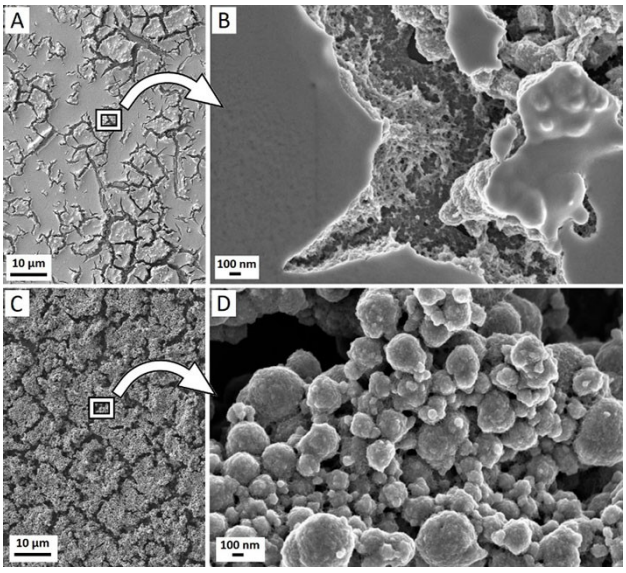

Figure 6. SEM pictures of **(A)** and **(B)**: Pt-PDA prepared by 'regular drying' of cyclohexanone in a fume hood (approx. 30 minutes); **(C)** and **(D)**: Pt-PDA prepared by 'prolonged drying' by covering the samples with watch glasses (maximum 8 hours).

Pt NPs in ethanol indicated a faster material formation which might be correlated to the less stable (partially sintered) Pt NPs redispersed in ethanol in comparison to cyclohexanone. In accordance, SEM of Pt-PDA prepared in ethanol (see Figure S8 in the Supporting Information) showed already for 'regular drying' a meso- and macroporous morphology formed by spherical beads, similar to the morphology observed for Pt-PDA prepared in cyclohexanone by 'prolonged drying' (Figure 6D). The spherules, however, appeared smaller and with a smoother surface which may reflect the lower fraction of ligands in the material prepared in ethanol, as discussed in section 2.3.4.

The morphologies of PDA-linked Pt NP networks depicted in Figure 6 turned out to be stable and insoluble in ethanol, i.e., they should withstand any vapors of VOCs (such as alcohols or hydrocarbons) that can be present in the atmosphere, as mentioned in section 2.2. For evidence, IR spectroscopy indicated that the coordinative bonding of amines and Pt NPs remained stable after 24 hours exposition to ethanol as well as to further organic solvents and water. Also, SEM of Pt-PDA prepared by both, 'regular' and 'prolonged drying' and stored in ethanol for 24 hours (see Figure S9 in the Supporting Information) revealed unaltered morphologies similar to Figure 6B and D.

2.4.2. Cross-Linking of Pt NPs with Different Bifunctional Ligands

In comparison to Pt-PDA, also the morphologies of the remaining four ligands cross-linked with Pt NPs were studied by SEM (see Figure 7 and Figure S10 in the Supporting Information). Always, both drying methods in cyclohexanone were employed during preparation ('regular drying' and 'prolonged drying').

As observed for Pt-PDA, SEM pictures of Pt-DAN and Pt-BEN prepared by 'regular drying' (see Figure S10a in the Supporting Information) revealed a heterogeneous structure with a flat and partially dense layer with wide cracks in which a buried, mesoporous structure (pore sizes of several 10 nm) became visible. In case of Pt-BEN, some small plate-like structures started to additionally form on its surface.

Also similar to the results of Pt-PDA, Pt-DAN and Pt-BEN prepared by 'prolonged drying' exhibited homogeneous meso- and macroporous structures which are shown in Figure 7A and B, respectively. While the morphology of Pt-DAN was built up by spherules (diameter several 100 nm), as for Pt-PDA, we observed flake-like structures (several 100 nm in diameter) for Pt-BEN, i.e., although DAN and BEN are structurally very similar (both diamines based on two aromatic rings), the cross-linked products differ significantly with respect to their macroscopic morphology. We note here as a reminder of section 2.3.4 that our studies on the formation rate of the ligand-linked networks also found significant differences between Pt-DAN (relatively slow) and Pt-BEN or Pt-PDA (relatively fast). The morphology that we found in SEM studies of Pt-DATER, however, indicates that it is probably not the formation rate which causes the formation of spherule- or flake-like morphologies:

In contrast to Pt-PDA, Pt-BEN and Pt-DAN, SEM pictures of Pt-DATER and Pt-DACH prepared by 'regular drying' showed already a meso- and macroporous structure (see Figure S10b in the Supporting Information), in accordance with the high formation rates that we found for Pt-DACH and Pt-DATER. The structure of Pt-DATER, however, is also built up by thin plate-like formations (several 100 nm in diameter), similar to that of Pt-BEN while the morphology of Pt-DACH is composed of almost perfect, individual spheres with diameters of several 100 nm. SEM samples of Pt-DATER and Pt-DACH prepared by 'prolonged drying' (Figure 7C and D) revealed that the morphologies did not change significantly when the reaction time was increased beyond that of 'regular drying'.

Given the similarities of the mesoporous morphologies of Pt-PDA, Pt-DACH and Pt-DAN on the one hand and Pt-BEN and Pt-DATER on the other hand, we speculate that structural details of the ligands may affect the macroscopic morphology of the ligand-linked network. It appears that more compact ligands (PDA, DACH, and DAN) promote the formation of meso- and macroscopic spherules while elongated ligands lead to the formation of more anisotropic, flake-like morphologies. We cautiously note here, however, that we found no indication for structural anisotropies of the ligand-linked Pt-DATER and Pt-BEN networks on molecular length scales studied by TEM (cf. section 2.1).

Overall, the SEM studies revealed that all materials developed meso- and macroporous morphologies after completion of the cross-linking reaction. Compared to a non-porous dense layer, these morphologies should be beneficial for the catalytic performance by improving the accessibility of reactant as well as by facilitating the dissipation of water of the hydrogen oxidation reaction. Furthermore, we found indications that the chemical structure of the ligands affects the appearance of the macroscopic morphology: The compact ligands in Pt-PDA, Pt-DAN and Pt-DACH showed spherical-like shapes while the

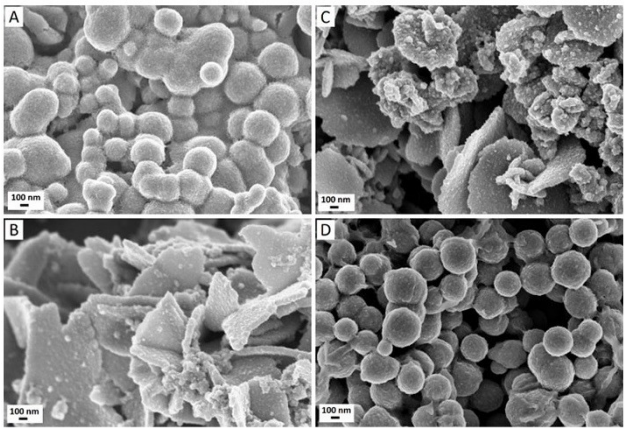

Figure 7. SEM pictures of **(A)**: Pt-DAN; **(B)**: Pt-BEN; **(C)**: Pt-DATER; **(D)**: Pt-DACH. All samples were prepared by 'prolonged drying' by covering the samples with watch glasses (maximum 8 hours).

elongated ligands in Pt-BEN and Pt-DATER exhibited plate-like structures.

3. Conclusions

In combination, the electron microscopy, infrared spectroscopy, and thermogravimetry data presented above show that all four aromatic bifunctional ligands (PDA, BEN, DATER and DAN) and also the non-aromatic but cyclic counterpart (DACH) can be employed to synthesize three-dimensional, cross-linked networks of Pt particles with diameters in the nanometer range. In accordance with our expectations, FTIR demonstrated that intact ligand molecules bind via their two amino groups to adjacent particles and act as spacers in the networks. As STEM tomography revealed, the interparticle distance directly reflects the ligand structure and can, thereby, be deliberately tuned. With the selection of ligands presented in this work, a variation of the inter-particle distances in the range of 0.8 to 1.4 nm was achieved and corresponded well to the nominal length of a single ligand molecule of the respective kind. All diamine ligands, in particular the aromatic ones, do not only act as rigid spacers but also provide thermally stable links within the networks and prevent the Pt nanoparticles from sintering. Pt NP networks linked by DATER, the longest and thermally most stable ligand within the selection of the present work, showed significant decomposition only well above 150 °C.

The fact that each Pt nanoparticle within the ligand-linked networks still exhibits many Pt surface sites available for adsorption, as evidenced by the CO band in the FTIR data, renders the networks particularly interesting for applications in catalysis where catalysts with a high density of active sites (the networks of the present study exhibit Pt contents of 44–56 wt.%) are required. A recent publication demonstrated high performance of the ligand-linked Pt NP networks presented in this work for catalytic hydrogen gas microsensors.[36] So far unprecedented, a very high sensitivity with a detection limit as low as 10 ppm hydrogen in combination with fast response times in the range of only 600–700 ms was achieved. In addition, ligand-linked Pt NP network catalysts were highly selective to hydrogen and showed no significant sensitivity to hydrocarbons.

Our SEM studies demonstrate that all five ligand-linked Pt NP networks develop meso- and macroporous morphologies if time for complete reaction between ligands and particles is allowed during synthesis. Such morphologies should be beneficial for the catalytic performance by improving the accessibility of reactants as well as by facilitating the dissipation of products such as water from hydrogen oxidation in the case of the hydrogen microsensors.

Two results of our comparative study appear particularly promising for deliberately tuning ligand-linked Pt NP networks for other applications in catalysis: On the one hand, the structure of the ligand molecules apparently affects the appearance of the macroscopic morphology. Compact ligands produced more compact, spherical aggregates while elongated ligands formed plate-like structures. On the other hand, the chemical structure of the ligands, predominantly but not only the distance of both amino groups, affected the microscopic network structure, namely the inter-particle distance. In that way transport of reactants and products within catalyst pores as well as steric demands on their adsorption and desorption, respectively, could potentially be tailored in a rational manner while maintaining high loadings of catalytically active Pt.

Acknowledgements

We thank E.-M. Meyer of the Institute for Microsensors, -actuators and -systems for acquiring the SEM images and K. Thiel of the Fraunhofer Institute for Manufacturing Technology and Advanced Materials, Bremen, Germany, for assistance with TEM measurements. This work has been supported by the German Research Foundation (Deutsche Forschungsgemeinschaft – DFG) via project number 299483494, "Ligand-linked platinum nanoparticles: a new material for gas sensors with high potential" (http://gepris.dfg.de/gepris/projekt/299483494).

Conflict of Interest

The authors declare no conflict of interest.

Keywords: Amines derivatives · bifunctional ligands · heterogeneous catalysis · nanoparticles · platinum

[1] T. Hübert, L. Boon-Brett, G. Black, U. Banach, *Sens. Actuators B* **2011**, *157*, 329–352.
[2] E. Menumerov, B. A. Marks, D. A. Dikin, F. X. Lee, R. D. Winslow, S. Guru, D. Sil, E. Borguet, P. Hutapea, R. A. Hughes, S. Neretina, *ACS Sens.* **2016**, *1*, 73–80.
[3] E. Brauns, E. Morsbach, S. Kunz, M. Bäumer, W. Lang, *Sens. Actuators B* **2014**, *193*, 895–903.
[4] Deutscher Bundestag, printed matter 19/20363, June **2020**.
[5] M. Nishibori, W. Shin, N. Izu, T. Itoh, I. Matsubara, *Sens. Actuators B* **2009**, 137, 524–528.
[6] I. Robins, F. Ross, J. E. A. Shaw, *J. Appl. Phys.* **1986**, *60*, 843–845.
[7] E. Morsbach, S. Kunz, M. Bäumer, *Catal. Sci. Technol.* **2016**, *6*, 339–348.
[8] E. Brauns, E. Morsbach, S. Kunz, M. Bäumer, W. Lang, *Sensors* **2014**, *14*, 20372–20381.
[9] E. Morsbach, E. Brauns, T. Kowalik, W. Lang, S. Kunz, M. Bäumer, *Phys. Chem. Chem. Phys.* **2014**, *16*, 21243–21251.
[10] B. Hvolbæk, T. V. W. Janssens, B. S. Clausen, H. Falsig, C. H. Christensen, J. K. Nørskov, *Nano Today* **2007**, *2*, 14–18.
[11] E. Morsbach, J. Spéder, M. Arenz, E. Brauns, W. Lang, S. Kunz, M. Bäumer, *Langmuir* **2014**, *30*, 5564–5573.
[12] S. B. Simonsen, I. Chorkendorff, S. Dahl, M. Skoglundh, J. Sehested, S. Helveg, *J. Am. Chem. Soc.* **2010**, *132*, 7968–7975.
[13] T. W. Hansen, A. T. Delariva, S. R. Challa, A. K. Datye, *Acc. Chem. Res.* **2013**, *46*, 1720–1730.
[14] X. Wang, P. Sonström, D. Arndt, J. Stöver, V. Zielasek, H. Borchert, K. Thiel, K. Al-Shamery, M. Bäumer, *J. Catal.* **2011**, *278*, 143–152.
[15] L. Altmann, S. Kunz, M. Bäumer, *J. Phys. Chem. C* **2014**, *118*, 8925–8932.
[16] S. Neumann, J. Schröder, F. Bizzotto, M. Arenz, A. Dworzak, M. Oezaslan, M. Bäumer, S. Kunz, *ChemNanoMat* **2019**, *5*, 462–471.
[17] Y. Choi, K. Tajima, W. Shin, N. Izu, I. Matsubara, N. Murayama, *J. Mater. Sci.* **2006**, *41*, 2333–2338.
[18] Y. Wang, J. Ren, K. Deng, L. Gui, Y. Tang, *Chem. Mater.* **2000**, *12*, 1622–1627.

[19] I. Schrader, J. Warneke, S. Neumann, S. Grotheer, A. A. Swane, J. J. K. Kirkensgaard, M. Arenz, S. Kunz, *J. Phys. Chem. C* **2015**, *119*, 17655–17661.
[20] J. R. Kremer, D. N. Mastronarde, J. R. McIntosh, *J. Struct. Biol.* **1996**, *116*, 71–76.
[21] David R. Lide, ed., CRC *Handbook of Chemistry and Physics*, Internet Version **2005**.
[22] T. Sheng, Y.-J. Qi, X. Lin, P. Hu, S.-G. Sun, W.-F. Lin, *Chem. Eng. J.* **2016**, *293*, 337–344.
[23] J. R. Errington, A. Z. Panagiotopoulos, *J. Chem. Phys.* **1999**, *111*, 21, 9731–9738.
[24] S. X. Huang, D. A. Fischer, J. L. Gland, *J. Vac. Sci. Technol. A* **1994**, *12*, 2164–2169.
[25] F. M. Hoffmann, *Surf. Sci. Rep.* **1983**, *3*, 107–192.
[26] M. Gajdoš, A. Eichler, J. Hafner, *J. Phys. Condens. Matter* **2004**, *16*, 1141–1164.
[27] H. M. Badawi, W. Förner, S. A. Ali, *Spectrochim. Acta Part A* **2013**, *112*, 388–396.
[28] S. Akyüz, T. Akyüz, N. M. Ozer, *J. Mol. Struct.* **2001**, *565–566*, 493–496.
[29] M. A. Azzem, U. S. Yousef, D. Limosin, G. Pierre, *J. Electroanal. Chem.* **1996**, *417*, 163–173.
[30] K. T. Wong, S. F. Bent, *J. Phys. Chem. C* **2013**, *117*, 19063–19073.
[31] M. J. Kappers, J. H. van der Maas, *Catal. Lett.* **1991**, *10*, 365–374.
[32] R. Pažout, J. Housková, M. Dušek, J. Maixner, P. Kačer, *Struct. Chem.* **2011**, *22*, 1325–1330.
[33] P. Tyagi, P. Gahlot, R. Kakkar, *Polyhedron* **2008**, *27*, 3567–3574.
[34] T. Mori, T. Hegmann, *J. Nanopart. Res.* **2016**, *18*, 295.
[35] W. Gao, W. T. Zheng, Q. Jiang, *J. Chem. Phys.* **2008**, *129*, 164705–164713.
[36] A. S. Pranti, D. Loof, S. Kunz, V. Zielasek, M. Bäumer, W. Lang, *Sensors & Actuators: B. Chemical* **2020**, *322*, 128619–128630; Actuators: B. Chemical **2020**, 322, 128619–128630.

Manuscript received: December 7, 2020
Revised manuscript received: June 3, 2021